Linking sand permeability anisotropy to fabric anisotropy via numerical simulation

Tokio Morimoto[1#], *Catherine* O'Sullivan[1], and *David M. G.* Taborda[1]

[1]*Imperial College London, Department of Civil and Environmental Engineering, London, UK*
[#]*Corresponding author: t.morimoto@imperial.ac.uk*

ABSTRACT

Characterisation of the permeability of soils is of practical importance and, for cohesionless or granular soils, it can be predicted from the void ratio and the particle size distribution (PSD). However, the effect of fabric anisotropy on the permeability is rarely discussed. Restricting consideration to granular (cohesionless) soil, this study combines a variety of numerical methods to investigate (1) how the anisotropy of the permeability evolves as the soil fabric anisotropy evolves in triaxial deformation and (2) establish a link between the anisotropy of the permeability and the fabric anisotropy. The Discrete Element Method (DEM) was employed to create linearly graded virtual samples of spheres (Cu of 1 to 2). Initially isotropic sphere packings were subjected to triaxial compression or triaxial extension up to 30% of absolute axial strain to induce an anisotropic fabric. Pore Network Models (PNMs) present a computationally efficient option for simulation of flow through the pore space. A PNM models fluid flow between pores (nodes) connected by pipes (edges) whose geometry is defined by the topology of the connected pores and the mass balance equation is solved at each pore. After demonstrating the accuracy of the PNM framework adopted here, this contribution presents data from PNM simulations that used the positions of individual particles in the sheared spherical packings as input data. The fabric and permeability anisotropies during triaxial shear deformation were compared at axial strain intervals of 1%. Detailed micro-scale analyses suggest that the anisotropy in the permeability can be attributed to an increase in the local conductance of fluid pipes in the direction of the major principal stress, which is related to the evolution of the pore topologies during the shear deformation.

Keywords: Permeability; Anisotropy; Fabric tensor; Pore Network Model; Computational Fluid Dynamics.

1. Introduction

Permeability (in $[m^2]$) or hydraulic conductivity (in $[m/s]$) is a fundamental soil property. For cohesionless or granular soils, empirical methods are often used to predict the permeability from the void ratio (e) and the particle size distribution (PSD) e.g. Hazen's method, and the Kozeny-Carman equation. These methods assume that the permeability of granular soils is isotropic. However, shear-induced permeability anisotropy has been observed in a few studies using analytical (Wong, 2003) and numerical (Kuhn et al., 2015) methods. Consideration of the permeability anisotropy has practical importance; for example, Wang (2021) showed that permeability anisotropy influences soil-pile interaction behaviour.

Over the past two decades the use of particle-scale numerical simulations in geomechanics has consistently increased as computational technology (both software and hardware) have improved. Particle-scale numerical studies can provide fundamental information which cannot be obtained from laboratory experiments. Only a few particle-scale numerical studies have specifically investigated anisotropy of permeability. Kuhn et al. (2015) studied the shear-induced evolution of the permeability anisotropy of granular particles and varied the particle shape by considering ellipsoids with different aspect ratios. Kuhn et al. (2015) completed a series of Discrete Element Method (DEM) simulations of biaxial plane strain compression with a constant mean stress. They extracted the positions of the particles and used the particle surfaces as boundary conditions in simulations of fluid flow through the pore space using the Lattice Boltzmann Method (LBM). Except for the case of highly elongated particles, they found no clear pattern to the evolution of the permeability anisotropy in a granular medium subjected to shear deformation. In the case of spherical particles, Kuhn et al. (2015) showed that the horizontal permeability was higher than the vertical permeability within a vertical strain range between 5% and 30% but lower within a vertical strain range between 30% and 50%. It is not clear why no clear permeability anisotropy was observed at larger strains even though the shear-induced contact normal anisotropy was evident. Shire et al. (2013), who also considered DEM simulations involving drained triaxial compression and extension of samples of spheres, reported a contrasting finding. They adopted a contact-based approach to partition the void space and observed that the constrictions orientated in the direction of the major principal stress tended to be larger, indicating that the permeability should also be greater in the direction of the major principal stress.

Developing upon these earlier works, this contribution investigates the evolution of the permeability anisotropy of initially isotropic granular materials using particle-scale simulations. Fully-resolved

Computational Fluid Dynamics (CFD) were carried out considering samples with isotropic packings. The CFD results were used to validate a less computationally expensive Pore Network Model (PNM). DEM simulations were then completed and used to generate input data for a series of PNM simulations. Combining data from the DEM and PNM simulations enabled the comparison between the evolution of the fabric and permeability anisotropies. This study also proposes a new tensor-based approach to quantify the permeability anisotropy in a granular material.

2. Methodology

2.1. Discrete Element Method (DEM)

2.1.1. Overview

The DEM was originally proposed by Cundall and Strack (1979). DEM is algorithmically similar to Molecular Dynamics (MD). A modified version of LAMMPS (Plimpton, 1995), an open-source MD/DEM code, was used to conduct DEM simulations. A simplified Hertz-Mindlin contact model was used.

2.1.2. Samples

Samples with four linear Particle Size Distributions (PSDs), whose coefficients of uniformity (Cu) were 1.01, 1.2, 1.5, and 2.0, were considered. Two sample sizes were considered for Cu = 1.01 and 2.0: for Cu = 1.01 there were 629 spheres in the "small" sample and 8,544 spheres in the "large" sample, while for Cu = 2.0 the "small" sample contained 497 spheres and the "large" sample comprised 12,787 spheres. For Cu = 1.2 and 1.5, only "small" samples were considered (629 and 491 particles, respectively). The PSDs of the small samples are shown in Figure 1.

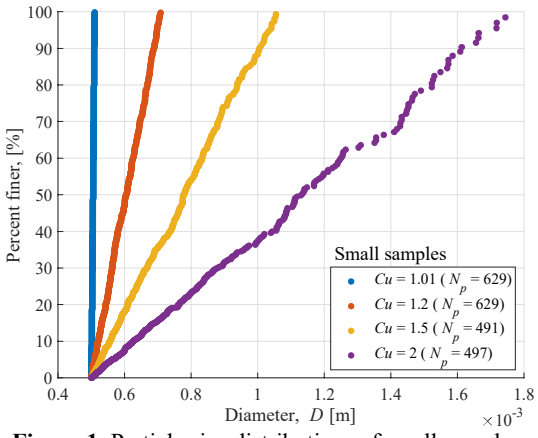

Figure 1. Particle size distributions of small samples. Reproduced from Morimoto et al. (2022b) under the terms of the CC-BY-4.0 licence.

2.1.3. Sample generation

For each PSD and sample size, a cloud of non-overlapping particles was generated using a random number generator under a cubical simulation domain enclosed by periodic boundaries. These were moved while keeping the stress state of the sample isotropic until an isotropic stress of 100 kPa was achieved. The particle friction coefficient during isotropic compression (μ_{iso}) was set to be 0.0 for the small samples while three μ_{iso} values ($\mu_{iso} = 0.01, 0.10, 0.29$) were considered for the large samples to obtain isotropic samples with a variety of void ratios.

Table 1. Properties of samples after isotropic compression.

Size	Cu	N_p	e	μ_{iso}
Small	1.01	629	0.536	0.00
	1.2	629	0.555	
	1.5	491	0.529	
	2.0	497	0.468	
Large	1.01	8 544	0.580	0.01
			0.652	0.10
			0.714	0.29
	2.0	12 787	0.486	0.01
			0.541	0.10
			0.586	0.29

2.1.4. Triaxial shear

To examine the evolution of fabric and permeability anisotropy during shear, triaxial shear was conducted for each isotopic sample. In this study, the z-direction is considered to be the "axial" direction and the x and y-directions are considered to be the "lateral" directions. The particle friction coefficient during triaxial shear (μ_{TX}) was set to be 0.3. During the triaxial shear deformation, the lateral normal stresses were maintained at 100 kPa and the periodic boundaries normal to the axial direction were moved at a constant strain rate of 5 %/s (for triaxial compression) or -5 %/s (for triaxial extension). The maximum axial strain amplitude was 10% for the small samples and 30 % for the large samples. The positions and radii of the particles and the boundary positions were output to conduct numerical analysis considering fluid flow outlined below.

2.1.5. Post-processing: Fabric tensor

The fabric tensor is often used to quantify the mechanical anisotropy of granular samples and the second order fabric tensor for contacts can be defined as:

$$f_{ij} = \frac{1}{N_c}\sum_{c=1}^{N_c} n_i^c n_j^c \qquad (1)$$

where N_c is the number of the contacts in the sample, and n_i^c is the unit vector expressing the direction of contact c. For each DEM sample considered in this study, the contact orientations were obtained by calculating the unit vectors connecting the centroids of each pair of contacting particles.

2.2. Fully-resolved CFD simulation (OF simulation)

2.2.1. Overview

In fully-resolved CFD, the mesh considered in the constant volume method simulations is sufficiently fine that the flow field within the pore space can be accurately obtained (fully-resolved). The meshing strategy employed by Knight et al. (2020) and Morimoto et al. (2022b) was used in this study. Specifically, this study used *MeshSpherePacking* (Knight, 2021), a meshing library, to generate the unstructured mesh of granular samples. The maximum mesh length was set to be 30 times smaller than the minimum particle diameter following Morimoto et al. (2022b); for fluid flow through regular packings this gives an accuracy above 88% when compared to the data in the analytical study carried out by Zick and Homsy (1982).

2.2.2. Simulation procedure

For each sample considered in the fully-resolved CFD simulations, the positions and radii of the spherical particles obtained from the DEM simulations were imported to *MeshSpherePacking* to generate the unstructured mesh representing the pore space of the sample. During the mesh generation, the particles crossing any periodic boundaries orthogonal to the direction in which fluid flow was considered were duplicated at the other side of the periodic boundary to conserve the void ratio of the sample (Figure 2). The unstructured mesh was then imported to *OpenFOAM*, an open-source CFD software (Weller et al., 1998). Within *OpenFOAM*, the *SimpleFOAM* algorithm, a steady-state incompressible flow solver, was used to solve the continuity and momentum equations.

One of x-, y-, and z-directions was chosen to be the flow direction. A constant velocity condition was considered at the inlet boundary, and the inlet velocity U was chosen to satisfy $Re < 1$ so that fluid flow in the pore space is fully-developed laminar flow. A constant pressure condition was considered at the outlet. At the surface of each particle, the no-slip condition was applied. Simulations conducted following the above procedure are called "*OF"* simulations hereinafter.

After the pressure field of a sample was obtained, the pressure at the inlet is exported. The pressure difference between the inlet and outlet, Δp, was related to the permeability of the sample (k) by

$$k = \frac{UA}{\mu}\frac{\Delta p}{L} \tag{2}$$

where A and L are cross-sectional area (in [m^2]) and length (in [m]) of the sample (Figure 2) and μ is the dynamic viscosity of the fluid phase in [Pa·s]. In this study, "permeability" has a unit of m^2 and is independent from the fluid dynamic viscosity.

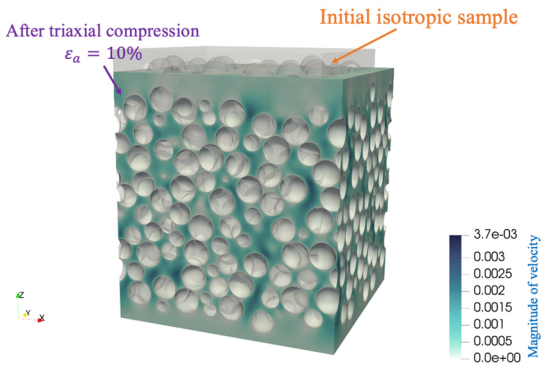

Figure 2. CFD simulation domain.

2.3. Pore Network Model

2.3.1. Overview

Pore Network Models (PNMs) are an efficient numerical method to consider fluid flow through granular or porous materials. In a PNM, the domain of a granular sample is discretised into pores. The connection between the pores is determined and considered as a pipe ("*throat*" hereinafter), where fluid can flow. Here, following Chareyre et al. (2012), the pore domain was discretised using a weighted Delaunay triangulation. The triangulation considered the particle centroids and a weight was assigned to each particle that equalled the square of the particle radius. Each of the resulting tetrahedra was taken to define a single pore. No merging stage was applied. The faces of the tetrahedra were used to identify the particle throats. Assuming the fluid flow to be incompressible and the particle positions to be static, mass conservation for pore a can be written as:

$$\sum_{b=1}^{4} Q_{ab} = 0 \tag{3}$$

where b is a neighbour of pore a and Q_{ab} is volumetric the flow rate from pore a to pore b in [m^3/s]. Applying Darcy's law, Q_{ab} is calculated as

$$Q_{ab} = \frac{G_{ab}}{\mu}(p_a - p_b) \tag{4}$$

where μ is the dynamic viscosity of the fluid in [Pa·s], p_a and p_b are the pressures of pores a and b in [Pa], G_{ab} is the "local" conductance (in [m^4]) of the fluid pipe connecting pores a and b.

The model used to calculate the local conductance determines the accuracy of the PNM. Morimoto et al. (2022b) proposed a "*HR4 model*" and showed that it gives a better overall agreement with local conductance values back-calculated from fully-resolved CFD simulations than other available models. According to the *HR4 model*, G_{ab} is formulated as

$$G_{ab} = 16\alpha\frac{\pi r_h^4}{l_{ab}} \tag{5}$$

where l_{ab}, r_h and α are the length, the hydraulic radius, and the shape factor of the fluid pipe, respectively. The hydraulic radius is defined as fluid volume divided by the solid surface area

$$r_h = \frac{V_{ab} - \sum_{m=1}^{3} V_m}{\sum_{m=1}^{3} \gamma_m} \quad (6)$$

where V_{ab} is the total volume of throat ab, V_m and γ_m are, respectively, the volume and surface area of the intersect of particle m and throat ab referring to Figure 4. The local throat void ratio is then calculated as

$$e^* = \frac{V_{ab} - \sum_{m=1}^{3} V_m}{\sum_{m=1}^{3} V_m} \quad (7)$$

The e^* value for each throat then determines the value of the shape factor, α, as

$$\alpha = 0.510\left(\frac{1}{1+e^*}\right)^3 - 0.565\left(\frac{1}{1+e^*}\right)^2 + 0.279\left(\frac{1}{1+e^*}\right) \quad (8)$$

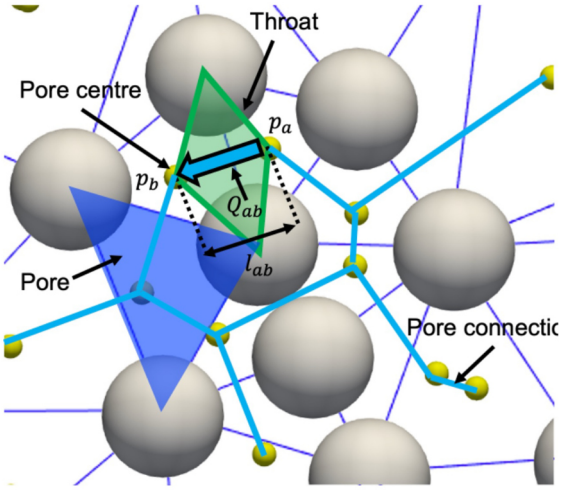

Figure 3. A schematic illustration of a pore network model in 2D for simplicity. Reproduced from Morimoto et al. (2022b) under the terms of the CC-BY-4.0 licence.

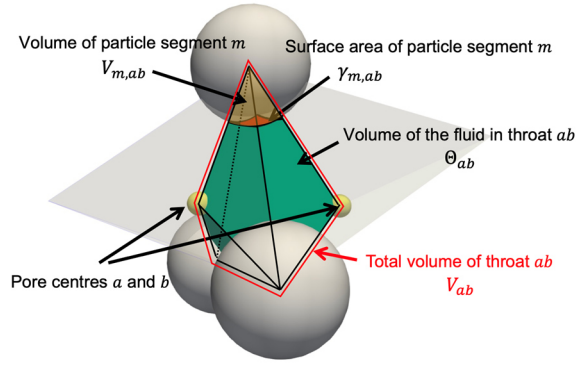

Figure 4. A schematic illustration of geometric parameters of a throat. Reproduced from Morimoto et al. (2022b) under the terms of the CC-BY-4.0 licence.

2.3.2. Simulation procedure

The flow direction was considered in one of x-, y-, and z- directions. The DEM particles crossing any periodic boundaries orthogonal to the direction in which fluid flow was considered were duplicated to be at the opposite side of the other side periodic boundary. The weighted Delaunay triangulation was conducted based on the positions and radii of the particles using *tetgen* (Si, 2015). Following Chareyre et al. (2012), the boundaries orthogonal to the direction in which fluid flow was considered were treated as spheres with a very large radius (termed "*boundary spheres*" hereinafter). Adjacent tetrahedra (pores) were identified from the Delaunay triangulation. The geometric properties (r_h, e^* and l_{ab}) of the adjacent tetrahedra (throats) were calculated to obtain their local conductance (G_{ab}).

The pressures for pores having a boundary sphere as their vertex ("*boundary pore*" hereinafter) were set to be 1 Pa if the boundary sphere corresponded to the inlet boundary or 0 Pa if the boundary sphere corresponded to the outlet boundary. Denoting the total number of pores as M and the number of boundary pores N, $M - N$ equations (Eq. (3) for the non-boundary pores) were considered for $M - N$ unknown variables (the pressure values of the non-boundary pores). The system of the equations was solved using a direct linear equation solver available in *PETSc* (Balay et al., 1997), and the pressure values of the pores were obtained.

The permeability of the samples was calculated based on Eq. (2). The volumetric flow rate through the sample ($Q = UA$ in Eq. (2)) can be calculated by summing the volumetric flow rates of the inlet and outlet boundary pores.

2.4. Tensor-based method to predict permeability

Morimoto et al. (2022b) proposed an alternative method to predict the global permeability of a granular sample from local conductances of the throats in the sample. This method was inspired by the Effective Medium Theory (EMT), which is proposed in Walton (1987) to predict the moduli of a granular sample from stiffnesses of contacts. The method also considered the contributions of Itasca (2007) and El Shamy et al. (2013) who predicted the global thermal conductivity in a granular sample from local thermal conductances between contacting particles in the sample. Just as Walton (1987) assumed that the local strain of springs representing contacting particles is equal to the global strain of the sample, Morimoto et al. (2022b) assumed the local pressure gradient for each fluid pipes to be equal to the global pressure gradient for the sample. Adopting this assumption, the global permeability tensor k_{ij} can be related to the local conductance (G^{fp}) and length (l^{fp}) of fluid pipe fp, and the unit vector representing the direction of fluid pipe fp (n_i^{fp}) as

$$k_{ij} = \frac{1}{V}\sum_{fp=1}^{N^{fp}} G^{fp}(l^{fp})^2 n_i^{fp} n_j^{fp} \quad (9)$$

where V is the total volume of the sample and N^{fp} is the number of fluid pipes existing in the system. The detailed derivation of Eq. (9) is given in Morimoto et al., 2022b).

As before, discretized pore space obtained via the weighted Delaunay triangulation was considered. The M values were calculated using Eq. (5) and then substituted into Eq. (9) to obtain the permeability tensor k_{ij}.

3. Comparison between fully-resolved CFD, PNM, and tensor-based method

In this section, the permeability data obtained from the fully-resolved CFD simulations, the PNM simulations, and the tensor-based method are compared. Computational cost considerations restricted the comparison to the "small" samples in Table 1.

Figure 5 presents the variations with Cu of axial and lateral permeability values obtained using each of the three methods at axial strain values of +10% (Figure 5(a)) and -10% (Figure 5(b)). For all the three methods, the axial permeability (k_{zz}) of the DEM sample at 10% of triaxial compression was higher than the lateral permeability (k_{xx}) of the sample (Figure 5(a)). Conversely, for the same magnitude of strain in extension, the lateral permeability exceeded the axial permeability as shown in Figure 5(b). These data are in agreement with the findings of Shire et al. (2013). In both Figure 5(a) and (b), the k values obtained from the PNM simulations agree with the k values obtained from the OF simulations. However, the tensor-based method overpredicted the k values for all the cases (Figure 5(a) and (b)). The overprediction can be attributed to the constant pressure gradient assumption made to derive Eq. (9). Such overprediction made by EMT has been also reported for the elastic moduli of samples (Makse et al. 1999; Khalili et al. 2017; Morimoto et al. 2022a).

The induced anisotropies are, however, small. Figure 6 compares the ratio of the axial to the lateral permeabilities obtained from the three methods. The average anisotropy in compression was 1.05, while the average anisotropy in extension was 0.85. No clear variation in the anisotropy with Cu can be observed. Nearly perfect agreement between the permeability ratios obtained from OF and PNM simulations was observed for TE samples. The results obtained from OF and PNM simulations for TC samples were similar although a relatively large discrepancy between the OF and PNM simulation results was observed for $Cu = 2$. The tensor-based method gave a similar result to the OF and PNM simulation result for the TE samples; however, this method tends to over-predict the permeability ratio of the TC samples.

The data on Figures 5 and 6 confirm that the PNM method adopted here is a reliable and efficient method to predict the permeability of granular samples for the range of Cu values and levels of deformation considered here. On the other hand, the tensor-based method can be used to qualitatively assess the permeability anisotropy of a sample but cannot predict accurately the permeability values of the sample.

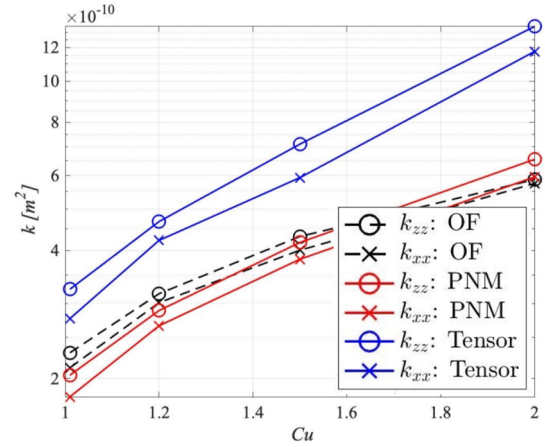

(a)

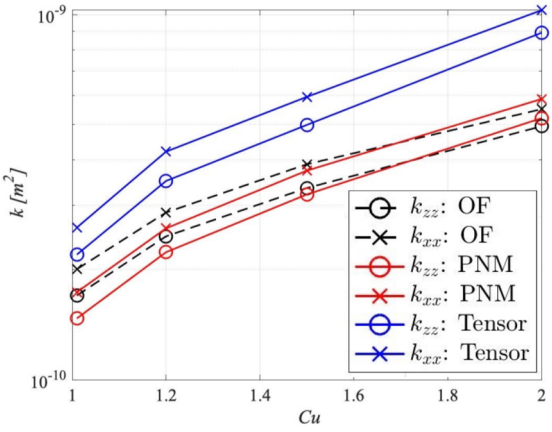

(b)

Figure 5. The axial (k_{zz}) and lateral (k_{xx}) permeability values of small DEM samples at different axial strain values for a variety of the Cu values (a) at an axial strain of 10% (TC10%) and (b) at an axial strain of -10% (TE10%).

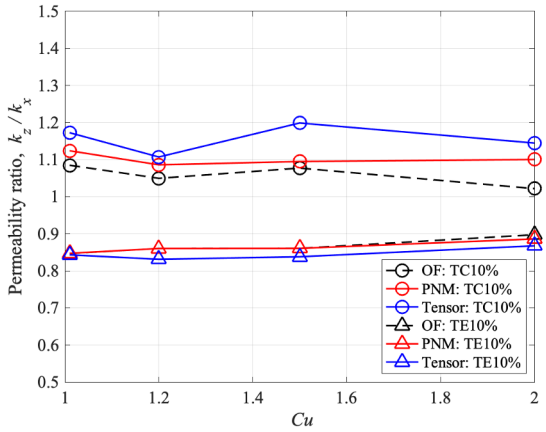

Figure 6. The ratio of the axial to the lateral permeabilities at different axial strain values for a variety of the Cu values.

4. Evolution of stress, fabric, and permeability anisotropies in samples

In the discussion of the evolutions of stress, fabric, and permeability anisotropies during triaxial shear only the "large" samples were considered. The contact normal fabric tensor was calculated following Eq. (1). The axial

and lateral permeabilities were determined via PNM simulations. The evolutions of the stress, fabric and permeability anisotropies in samples with Cu = 1.01 during triaxial compression and extension are plotted in Figure 7 ((a) for a dense sample and (b) for a loose sample). In all cases, the stress, fabric, and permeability ratios were >1.0 during triaxial compression and <1.0 during triaxial extension, which indicates a correlation between the three measures of anisotropy.

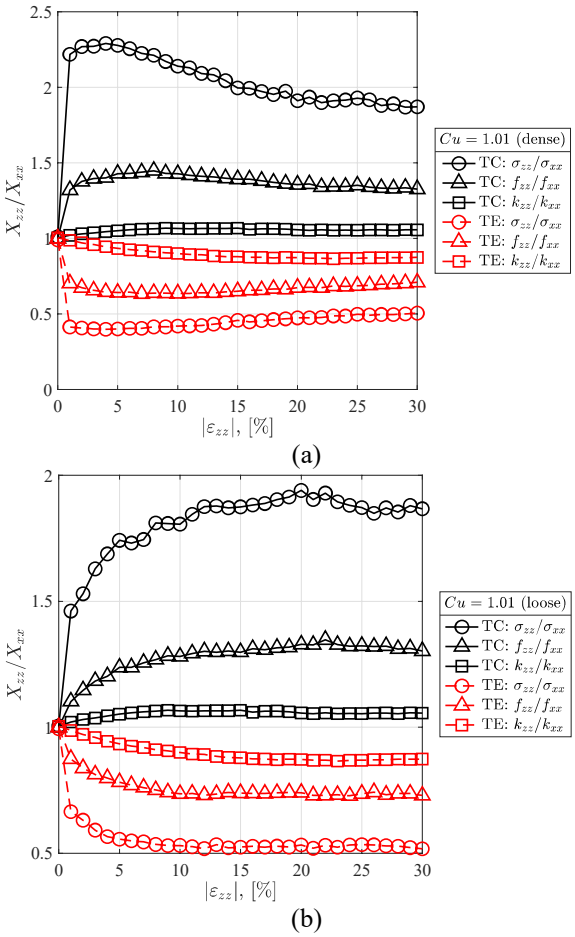

Figure 7. The evolution of stress, fabric, and permeability anisotropies in the sample with Cu = 1.01 during TC and TE loadings for (a) the dense sample (e = 0.580) and (b) the loose sample (e = 0.714).

Morimoto et al. (2022a) showed that the stiffness and thermal conductivity of granular materials can be related via the fabric tensor and the thermal conductivity tensor proposed in Itasca (2007). It is reasonable to conclude that the stiffness anisotropy can also be related to the permeability anisotropy. To examine the hypothesis, the evolutions of the fabric and permeability anisotropy ratios in the sample with Cu = 1.01 during triaxial shear are compared in Figure 8. It demonstrates that steady-state fabric and permeability anisotropy ratios exist: $(f_{zz}/f_{xx})_{steady} \cong 1.3$ and $(k_{zz}/k_{xx})_{steady} \cong 1.05$ for triaxial compression, while $(f_{zz}/f_{xx})_{steady} = 0.7$ and $(k_{zz}/k_{xx})_{steady} \cong 0.87$ for triaxial extension. The data on Figure 8 show that the relationship between the fabric anisotropy and the permeability anisotropy is not unique but it depends on the sample density. The permeability anisotropy evolved more slowly than fabric anisotropy; for the TE samples, the permeability anisotropy ratio continuously decreases while the fabric anisotropy ratio maintains a similar value.

Data on the three measures of anisotropy for the samples with Cu = 2.0 are presented on Figure 9. Just as was the case for the samples with Cu = 1.01, the fabric and permeability anisotropy ratios of the samples with three different densities reached similar values. Steady-state fabric and permeability anisotropy ratios of the samples with Cu = 2.0 were very similar to those of the samples with Cu = 1.01.

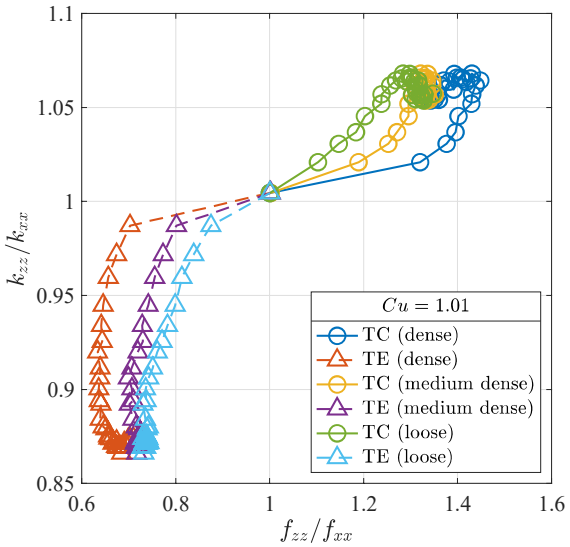

Figure 8. The permeability anisotropy ratio versus the fabric anisotropy ratio (Cu = 1.01). Plotted per ±1% axial strain.

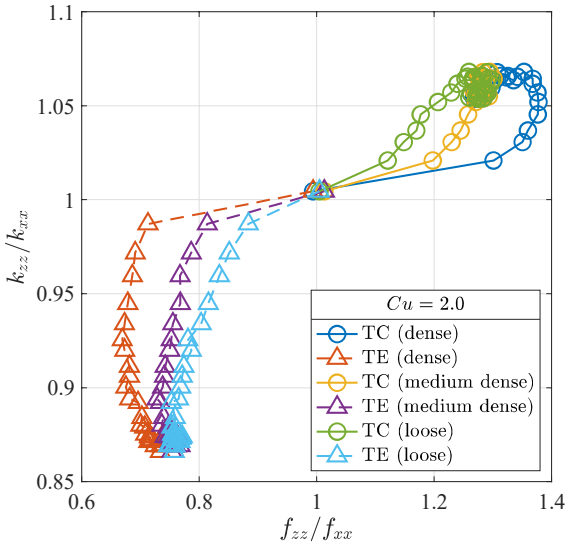

Figure 9. The permeability anisotropy ratio versus the fabric anisotropy ratio (Cu = 2.0). Plotted per ±1% axial strain.

5. Rose diagrams of local mechanical and hydrodynamic properties

A better understanding of the permeability anisotropy can be obtained using rose diagrams. In Eq. (9), the term $G^{fp}(l^{fp})^2$ quantifies the shape of the throat, while the term n_i^{fp} gives the throat orientation. By considering the

statistical distribution of n_i^{fp}, a rose diagram for the local conductances of throats in a sample can be created.

Figure 10 shows the two rose diagrams for the sample with Cu = 1.01 after triaxial compression to $\varepsilon_{zz} = 30\%$). Figure 10(a) is the rose diagram expressing the fabric tensor and each bin is coloured based on the contact normal force normalised by the averaged contact normal force following Shire et al. (2013); there is clearly a preferential orientation for the contact normal vectors in the direction of the major principal stress. Figure 10(b) shows the rose diagram of the throat normal vectors where each bin is coloured by the magnitude of $G^{fp}(l^{fp})^2$. In contrast to the case for the contact normals, the anisotropy in the direction of the throat normal vectors is not significant even after triaxial compression; however, there is a clear bias in the magnitude of $G^{fp}(l^{fp})^2$ in the direction of the major principal stress. The data on Figure 10(b) show that the permeability anisotropy observed in Figure 7 can be attributed to the change in the shape of the throats rather than the change in the direction of the throats.

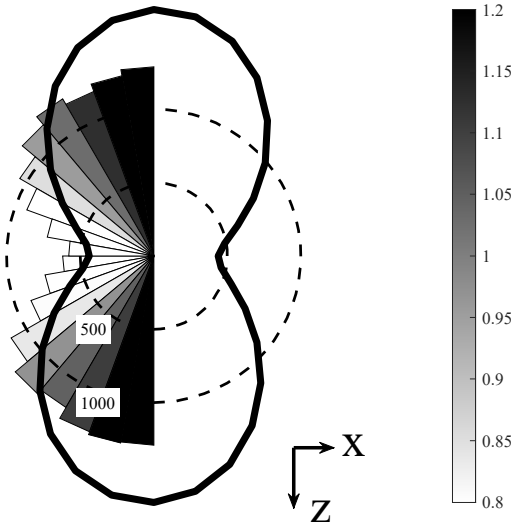

(a)

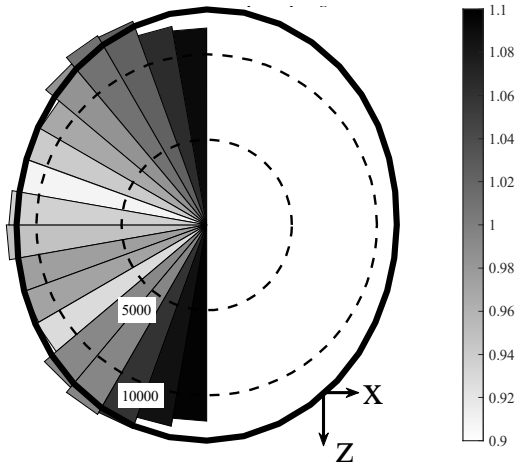

(b)

Figure 10. Rose diagrams of (a) contact normal vectors and (b) throat normal vectors in a sample with Cu = 1.01 at an axial strain of 30% (Triaxial compression).

Figure 11 shows the rose diagrams for the sample after triaxial extension ($\varepsilon_{zz} = -30\%$). A significant anisotropy in terms of the direction of the contact normal vectors was observed in Figure 11(a); again, these are orientated in the direction of the major principal stress. On the other hand, the shape of the rose diagram for the throats (Figure 11(b)) was nearly circular (i.e. isotropic) and there is a clear bias in the $G^{fp}(l^{fp})^2$ values, so that the pores with the larger values of $G^{fp}(l^{fp})^2$ tend to be orientated in the direction of the major principal stress.

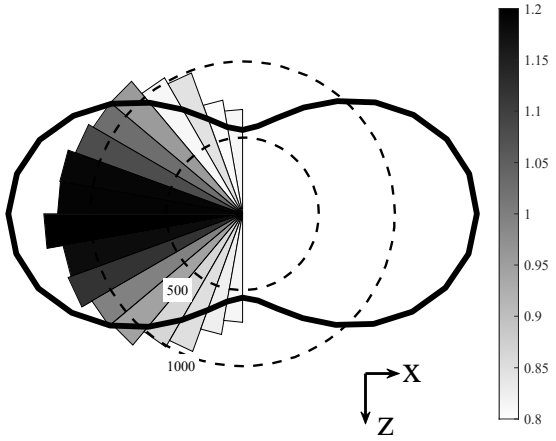

(a)

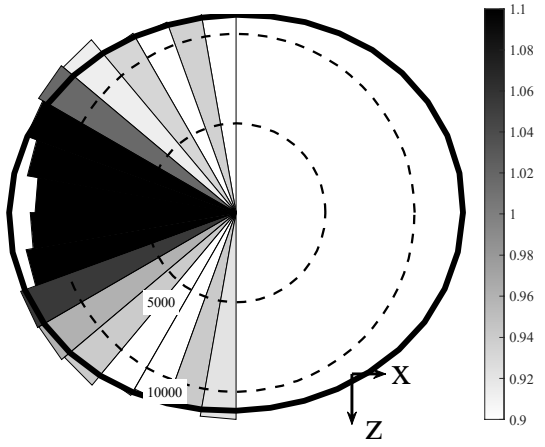

(b)

Figure 11. Rose diagrams of (a) contact normal vectors and (b) throat normal vectors in a sample with Cu = 1.01 at an axial strain of -30% (Triaxial extension).

6. Conclusions

This study considered the evolution of the anisotropy in granular samples in terms of contact normal, fabric and permeability using three types of numerical method. Fully-resolved CFD simulations were conducted for samples with around 500 particles and Cu values ranging from 1.01 to 2.00 to validate a Pore Network Model (PNM) and a tensor-based method. For each of the methods applied, the permeability value of the sample in the major stress direction was higher than that in the minor stress direction. The PNM, which is significantly more computationally efficient than the fully-resolved CFD, gave similar permeability values to those obtained

from the fully-resolved CFD. However, the tensor-based method over-predicted the permeability values, although the ratio of the axial to the lateral permeabilities was well-captured with the method.

The evolution of the fabric and permeability anisotropies was compared using the validated PNM. Although the directions of the fabric and permeability anisotropies coincided, the corresponding steady-state values were different. In addition, it was found that the permeability anisotropy ratio grew more slowly than the fabric anisotropy ratio. This result suggested that these two anisotropies cannot be directly associated.

The microscopic mechanical and hydrodynamic anisotropies of the samples after triaxial compression and extension were visualised using rose diagrams. While the direction of the contact normal vectors exhibited a significant anisotropy, the anisotropy in the orientations of the throats (fluid pipes) was not noticeable. However, there was an increase in local conductance values of the sample in the major stress direction, which explains the increase in the global permeability in the direction of the major principal stress for these samples which are initially perfectly isotropic.

Acknowledgements

Tokio Morimoto was funded by the European Union's Horizon 2020 research and innovation program Marie Skłodowska-Curie grant agreement MATHEGRAM No. 813202. DEM and OpenFOAM simulations were conducted on the Research Computing Service facilities at Imperial College London (DOI: 10.14469/hpc/2232).

References

Balay, S., Gropp, W.D., McInnes, L.C., and Smith, B.F., 1997. "Efficient management of parallelism in object-oriented numerical software libraries." In *Modern Software Tools for Scientific Computing*, edited by E. Arge, A. M. Bruaset, and H. P. Langtangen. 163–202. Boston, MA, US. https://doi.org/10.1007/978-1-4612- 1986-6_8.

Chareyre, B., Cortis, A., Catalano, E., andBarthélemy, E. 2012. "Pore-scale modeling of viscous flow and induced forces in dense sphere packings." Transport in porous media, 94(2), 595-615. https://doi.org/10.1007/s11242-012-0057-2

Cundall, P.A., and Strack, O.D.L., 1979. "A discrete numerical model for granular assemblies." Géotechnique 29 (1), 47–65. https://doi.org/10.1680/geot.1979.29.1.47

El Shamy, U., De Leon, O., and Wells, R. 2013. "Discrete element method study on effect of shear-induced anisotropy on thermal conductivity of granular soils." Int. J. Geomech. 13 (1). 57–64. https://doi.org/10.1061/(ASCE)GM.1943-5622.0000165.

Itasca. 2007. PFC3D version 4.0 user manual. Minneapolis: Itasca Consulting Group.

Khalili, M. H., Roux, J.N., Pereira, J.M., Brisard, S., and Bornert, M. 2017. "Numerical study of one-dimensional compression of granular mate- rials. II. Elastic moduli, stresses, and microstructure." Phys. Rev. E 95 (3): 032908. https://doi.org/10.1103/PhysRevE.95.032908.

Knight, C., 2021. mesh-sphere-packing. https://github.com/chrisk314/mesh-sphere- packing.

Knight, C., O'Sullivan, C., van Wachem, B., and Dini, D., 2020. "Computing drag and interactions between fluid and polydisperse particles in saturated granular materials." Comput. Geotech. 117, 103210. https://doi.org/10.1016/j.compgeo.2019.103210.

Kuhn, M.R., Sun, W.C., and Wang, Q. 2015. "Stress-induced anisotropy in granular materials: fabric, stiffness, and permeability." Acta Geotechnica 10(4), 399-419. https://doi.org/10.1007/s11440-015-0397-5

Makse, H. A., Gland, N., Johnson, D. L., and Schwartz, L. M. 1999. "Why effective medium theory fails in granular materials." Phys. Rev. Lett. 83 (24): 5070. https://doi.org/10.1103/PhysRevLett.83.5070.

Morimoto, T., O'Sullivan, C., and Taborda, D. M. 2022a. "Exploiting DEM to Link Thermal Conduction and Elastic Stiffness in Granular Materials." Journal of Engineering Mechanics, 148(2), 04021139. https://doi.org/10.1061/(ASCE)EM.1943-7889.0002054

Morimoto, T., Zhao, B., Taborda, D. M., and O'Sullivan, C. 2022b. "Critical appraisal of pore network models to simulate fluid flow through assemblies of spherical particles." Computers and Geotechnics, 150, 104900. https://doi.org/10.1016/j.compgeo.2022.104900

Plimpton, S. 1995. "Fast parallel algorithms for short-range molecular dynamics." Journal of Computational Physics, 117(1), 1–19. https://doi.org/10.1006/jcph.1995.1039

Shire, T., O'Sullivan, C., Barreto, D., and Gaudray, G. 2013. "Quantifying stress-induced anisotropy using inter-void constrictions." Géotechnique 63(1), 85-91. https://doi.org/10.1680/geot.11.T.020

Si, H., 2015. "TetGen, a Delaunay-based quality tetrahedral mesh generator." ACM Trans. Math. Software (TOMS) 41 (2), 1–36. https://doi.org/10.1145/2629697.

Walton, K. (1987). The effective elastic moduli of a random packing of spheres. Journal of the Mechanics and Physics of Solids, 35(2), 213-226. https://doi.org/10.1016/0022-5096(87)90036-6

Wang, L. 2021. "Vertical response of a pile embedded in highly-saturated soil with compressible pore fluid and anisotropic permeability." Computers and Geotechnics, 140, 104462. https://doi.org/10.1016/j.compgeo.2021.104462

Weller, H.G., Tabor, G., Jasak, H., and Fureby, C. 1998. "A tensorial approach to computational continuum mechanics using object-oriented techniques." Comput. Phys. 12 (6), 620–631. https://doi.org/10.1063/1.168744.

Wong, R.C.K. 2003a. "A model for strain-induced permeability anisotropy in deformable granular media." Canadian Geotechnical Journal. 40(1), 95-106. https://doi.org/10.1139/t02-088

Wong, R.C.K. 2003b. "Strain-induced anisotropy in fabric and hydraulic parameters of oil sand in triaxial compression." Canadian Geotechnical Journal. 40(3), 489-500. https://doi.org/10.1139/t03-005

Zick, A.A., and Homsy, G.M., 1982. "Stokes flow through periodic arrays of spheres." J. Fluid Mech. 115, 13–26. https://doi.org/10.1017/S0022112082000627.